

Electro-vortex flow simulation using coupled meshes

Weber, N.; Beckstein, P.; Galindo, V.; Starace, M.; Weier, T.;

Originally published:

March 2018

Computers & Fluids 168(2018), 101-109

DOI: <https://doi.org/10.1016/j.compfluid.2018.03.047>

Perma-Link to Publication Repository of HZDR:

<https://www.hzdr.de/publications/Publ-25910>

Release of the secondary publication
on the basis of the German Copyright Law § 38 Section 4.

CC BY-NC-ND

Electro-vortex flow simulation using coupled meshes

Norbert Weber, Pascal Beckstein, Vladimir Galindo, Marco Starace, Tom Weier

Helmholtz-Zentrum Dresden - Rossendorf, Dresden, Germany

Abstract

A numerical model for simulating electro-vortical flows in OpenFOAM is developed. Electric potential and current are solved in coupled solid-liquid conductors by a parent-child mesh technique. The magnetic field is computed using a combination of Biot-Savart's law and induction equation. Further, a PCG solver with special regularisation for the electric potential is derived and implemented. Finally, a performance analysis is presented and the solver is validated against several test cases.

Keywords: electro-vortex flow, OpenFOAM, coupled parent child mesh

1. Introduction

Electro-vortex flow is highly relevant in many industrial processes. Possible applications span from electromagnetic stirring [1] for grain size reduction in solidification [2, 3] over electrode welding [4], electroslag welding, electroslag (re-)melting [5, 6], vacuum arc melting [7] to electrolytic reduction (of e.g. aluminium [8]). Further, many technical devices, as liquid fuses [9], electric jet engines, arc furnaces [10] and liquid metal batteries [11, 12, 13] involve or rely on electro-vortex flows. For an overview about such flows, see [14, 15, 16].

Electro-vortex flow is not an instability. It develops at (or near) a changing cross-section of a (liquid) conductor. Radial currents produce, together with their own magnetic field, a Lorentz force, which is non-conservative, i.e. its curl is not equal to zero. This force cannot be compensated totally by a pressure

13 gradient and therefore drives a flow. For an illustrative example, see Shercliff
14 [17].

15 Numerical simulation of electro-vortex flow is easy when modelling only the
16 fluid, or a non-conducting obstacle inside a fluid. However, in most realistic
17 cases, electric current passes from solid to liquid conductors and vice versa.
18 The electric potential in these regions must therefore be solved in a coupled
19 way. The classical, segregated approach means solving an equation in each
20 region, and coupling the potential only at the interfaces by suitable boundary
21 conditions [11]. While that is easy to implement, convergence is rather poor.
22 An implicit coupling of the different regions by block matrices is a sophisticated
23 alternative for increasing convergence [18]. However, it is memory-intensive and
24 by no means easy to implement.

25 In this article we will present an alternative effective option for region cou-
26 pling in OpenFOAM. We solve global variables (electric potential, current den-
27 sity) on a global mesh with a variable electric conductivity according to the
28 underlying material. We then map the current density to the fluid regions and
29 compute the electromagnetic induced flow there. This parent-child mesh tech-
30 nique was already used for the similar problem of thermal conduction [19, 20]
31 and just recently for the solution of eddy-current problems with the finite volume
32 method [21].

33 **2. Mathematical and numerical model**

34 *2.1. Overview*

The presented multi-region approach is based on a single phase incompressible magnetohydrodynamic (MHD) model [22, 11]. The flow in the fluid is described by the Navier-Stokes equation (NSE)

$$\frac{\partial \mathbf{u}}{\partial t} + (\mathbf{u} \cdot \nabla) \mathbf{u} = -\nabla p + \nu \Delta \mathbf{u} + \frac{\mathbf{J} \times \mathbf{B}}{\rho}, \quad (1)$$

with \mathbf{u} denoting the velocity, t the time, p the modified pressure, ν the kinematic viscosity and ρ the density. We split the electric potential ϕ , the current density

\mathbf{J} and the magnetic field \mathbf{B} into a constant (subscript 0) and induced part (lower case) as

$$\phi = \phi_0 + \varphi \quad (2)$$

$$\mathbf{J} = \mathbf{J}_0 + \mathbf{j} \quad (3)$$

$$\mathbf{B} = \mathbf{B}_0 + \mathbf{b}. \quad (4)$$

In order to determine the distribution of the constant part of the electric potential ϕ_0 we solve a Laplace equation for the electric potential

$$\nabla \cdot \sigma \nabla \phi_0 = 0 \quad (5)$$

on the global mesh. The above equation is obtained starting from the Kirchhoff law of charge conservation ($\nabla \cdot \mathbf{J}_0 = 0$) and $\mathbf{J}_0 = -\sigma \nabla \phi_0$. Note that the conductivity σ is a field and not a constant, because the equation is solved on the full geometry. The global current density is then calculated as

$$\mathbf{J}_0 = -\sigma \nabla \phi_0 \quad (6)$$

35 and mapped to the fluid region. Afterwards, the constant magnetic field is
36 determined as described in section 2.1.1 only in the fluid.

Often it is sufficient to calculate only the constant current and magnetic field. Nevertheless, our solver also allows to compute their induced counterparts, e.g. for simulating the Tayler instability [23, 24, 25]. The scheme is similar to that described above: in a first step, the induced electric potential φ is determined by solving a Poisson equation

$$\nabla \cdot \sigma \nabla \varphi = \nabla \cdot \sigma (\mathbf{u} \times \mathbf{B}) \quad (7)$$

after mapping the source term $\mathbf{u} \times \mathbf{B}$ to the global mesh. The induced current can be computed taking into account Ohm's law

$$\mathbf{j} = \sigma (-\nabla \varphi + \mathbf{u} \times \mathbf{B}). \quad (8)$$

37 After mapping \mathbf{j} to the fluid mesh we determine the induced magnetic field as
38 described in section 2.1.1.

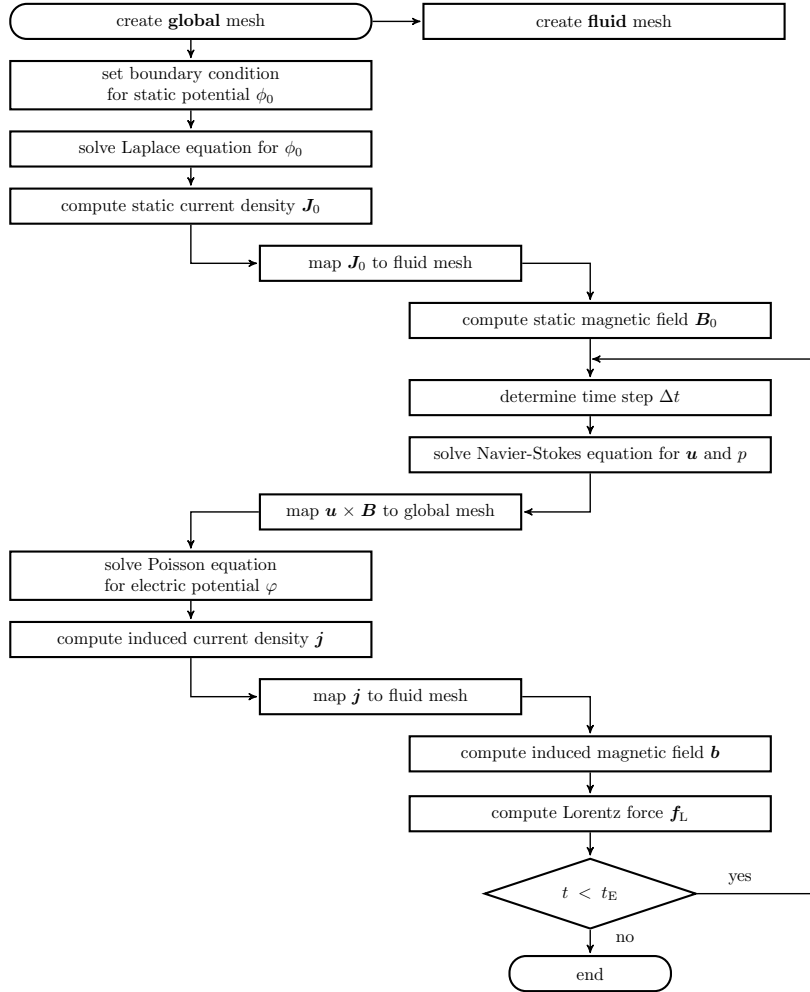


Figure 1: Flowchart of the simulation model.

39 Our model is not capable of describing AC currents, because we use the
 40 quasi-static approximations by neglecting the temporal derivation of the vector
 41 potential ($d\mathbf{a}/dt = 0$) and magnetic field ($d\mathbf{b}/dt = 0$) [26]. For a detailed
 42 flowchart of the model, please refer to figure 1.

43 2.1.1. Computation of the magnetic field

For the computation of both, the constant part of the magnetic field \mathbf{B}_0 and
 its induced counterpart \mathbf{b} we use the inversion of Ampères law, the Biot-Savart

integral

$$\mathbf{B}(\mathbf{r}) = \frac{\mu_0}{4\pi} \int \frac{\mathbf{J}(\mathbf{r}') \times (\mathbf{r} - \mathbf{r}')}{|\mathbf{r} - \mathbf{r}'|^3} dV' \quad (9)$$

44 to determine both from the current density \mathbf{J} . This integro-differential approach
 45 was proposed by Meir and Schmidt [27, 28, 29, 30, 31, 32] and later used for
 46 describing dynamos [33, 34, 35] and the Tayler instability [22].

47 In order to obtain the magnetic field in one single cell (at the position \mathbf{r}),
 48 the electric current densities of all other cells (at the position \mathbf{r}') have to be
 49 integrated. The number of operations is therefore equal to the number of cells
 50 squared. This way of computation is extremely costly. We will explain here
 51 several ways for a speed up of the procedure. Solving Biot-Savart's integral on
 52 a coarser grid, recalculating it every n th time step, and an appropriate paral-
 53 lellisation [22] are the most simple ways.

54 The parallelisation is implemented in OpenFOAM using MPI. Basically, each
 55 processor contains only the current density of its *local* cells. With this, it com-
 56 putes the magnetic field for the *full* geometry (see figure 2a). Finally, the field
 57 \mathbf{B} of each cell has to be summed up over all processors. This might be done
 58 using the MPI function ALLREDUCE, resulting in a correct and global \mathbf{B} on
 59 all processors. However, this is not necessary, because a single processor needs
 60 only its *local* \mathbf{B} for further computation. Therefore, each processor receives only
 61 its *local* magnetic field from all other processors and adds up all contributions
 given. The communication process is illustrated in figure 2b.

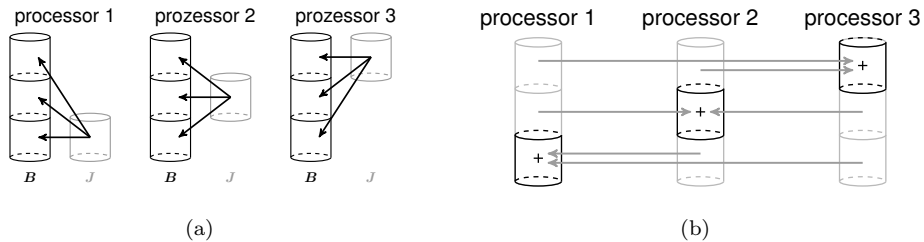


Figure 2: Each processor computes a full magnetic field from its local current \mathbf{J} (a), receives afterwards only its local \mathbf{B} from all other processors and adds it up (b).

62

Increasing the speed-up considerably is possible by computing Biot-Savart's

integral only on the boundaries and solving the induction equations [36, 37]

$$0 = \Delta \mathbf{B}_0 \quad (10)$$

$$0 = \frac{1}{\sigma \mu_0} \Delta \mathbf{b} + \nabla \times (\mathbf{u} \times \mathbf{B}) \quad (11)$$

63 for the constant and induced magnetic field in the quasi-static limit [26].

An even faster alternative is shifting the problem from the magnetic field \mathbf{B} to the vector potential \mathbf{A} using the relation $\mathbf{B} = \nabla \times \mathbf{A}$. Similar to Biot-Savart's law for \mathbf{B} , the vector potential can be determined by Green's identity [38]:

$$\mathbf{A}(\mathbf{r}) = \frac{\mu_0}{4\pi} \int \frac{\mathbf{J}(\mathbf{r}')}{|\mathbf{r} - \mathbf{r}'|} dV'. \quad (12)$$

64 Please note that this formula is much cheaper to compute than Biot-Savart's
65 law (equation 9) [39, 40].

The transport equations for the vector potential are derived from Ampère's law, $\mathbf{B} = \nabla \times \mathbf{A}$, Ohm's law [41] and using the Coulomb gauge condition $\nabla \cdot \mathbf{A} = 0$ as

$$0 = \frac{1}{\sigma \mu_0} \Delta \mathbf{A}_0 - \nabla \phi_0 \quad (13)$$

$$0 = \frac{1}{\sigma \mu_0} \Delta \mathbf{a} + \mathbf{u} \times (\mathbf{B}_0 + \nabla \times \mathbf{a}) - \nabla \varphi. \quad (14)$$

66 Calculating the magnetic field by Biot-Savart's integral (equation 9) gives
67 the most accurate result but takes very long. Solving a transport equation
68 for \mathbf{A} or \mathbf{B} or computing $\mathbf{B} = \nabla \times \mathbf{A}$ always induces a certain numerical
69 error when calculating the gradients. However, combining Green's identity with
70 the transport equation for the vector potential is very fast. We will therefore
71 compute the large and static magnetic field \mathbf{B}_0 by Biot-Savarts law and the
72 weak induced field \mathbf{b} by Green's identity and equation (14).

73 3. Discretisation

74 Special attention must be paid to the discretisation of the Laplace term
75 $\nabla \cdot (\sigma \nabla \phi)$ of equation 5 and 7 because of the sharp jump in conductivity between

76 different materials. A linear interpolation of σ would lead to a wrong potential
77 near the interface.

For a consistent application of the Gauss theorem to discretise the equations, the electric conductivity is interpolated harmonically. Knowing that the potential ϕ_f and the normal current $(\mathbf{j} \cdot \mathbf{n})_f$ must be continuous from a cell P to its neighbour N , we find the conductivity at the face f to be

$$\sigma_f = \left(\frac{(\delta_P/\delta)}{\sigma_P} + \frac{(\delta_N/\delta)}{\sigma_N} \right)^{-1} \quad (15)$$

78 with δ_i denoting the distance cell centre - face and δ the distance between
79 both cell centres. In the quasi-static limit, this exactly matches the embedded
80 discretisation scheme which was derived in [21] to get a proper discretisation of
81 the Laplacian.

Secondly, care must be taken when computing the gradient of the potential to determine the current density as $\mathbf{J} = -\sigma \nabla \phi$. In order to be able to use the Gauss theorem for discretisation, the electric potential on the faces must be determined. Using the same assumptions as for the harmonic interpolation described above, we identify the electric potential at the face as

$$\phi_f = w\phi_P + (1-w)\phi_N \quad (16)$$

with the interpolation weight

$$w = \frac{\delta_N \sigma_P}{\delta_P \sigma_N + \delta_N \sigma_P}. \quad (17)$$

82 As before, this interpolation scheme corresponds to the embedded discretisation
83 of the gradient from [21] in case of the quasi-static assumption. All other
84 discretisation schemes do not need special attention.

85 4. Equation solvers

86 The solution procedure of our model is illustrated in figure 1. As the Navier-
87 Stokes equation is discretised and solved by means of the PISO-algorithm [42],
88 three different Poisson equations need to be addressed within each time step.

89 This comprises the Laplace equation for the static potential ϕ_0 , one Poisson
90 equation for the potential φ and another Poisson equation for the fluid pressure
91 p . Especially the latter two are most commonly solved for Neumann boundary
92 conditions. To improve the overall robustness of the solution process in connec-
93 tion with the employed parent-child mesh approach, we have implemented an
94 alternative regularisation technique for the iterative equation solvers in Open-
95 FOAM, which is briefly explained in the following.

The discretisation of a Poisson equation leads to a linear equation system

$$\mathbf{M}\boldsymbol{\psi} = \mathbf{r}, \quad (18)$$

96 where $\mathbf{M} \in \mathbb{R}^{n \times n}$ is a symmetric positive semi-definite matrix, $\boldsymbol{\psi} \in \mathbb{R}^n$ is the
97 discrete solution vector for either φ or p , and the right-hand side $\mathbf{r} \in \mathbb{R}^n$ mainly
98 represents the inhomogeneous part. Each row of the system (18) is related to one
99 of n cells. In case of a Neumann problem, the system matrix will be singular and
100 the solution is only defined up to an additive constant vector. More specifically,
101 the one-vector $\mathbf{1} = (1, 1, \dots, 1, 1)^T$ lies in the null space of the linear map $\mathbf{M}\boldsymbol{\psi}$.
102 In other words, $\mathbf{v}_1 = \mathbf{1}/\sqrt{n}$ is a normalized eigenvector corresponding to the
103 eigenvalue $\lambda_1 = 0$ in accordance with the identity $(\mathbf{M} - \lambda_1 \mathbf{I})\mathbf{v}_1 = \mathbf{0}$.

In OpenFOAM such a singular matrix \mathbf{M} is regularised by means of adding
the equation

$$c_R \psi_P = c_R \psi_R \quad (19)$$

104 to the row which belongs to cell P , where c_R is initially an arbitrary coefficient,
105 ψ_P is the unknown solution and ψ_R is a reference solution for that cell. In
106 order to slightly increase diagonal dominance of \mathbf{M} , c_R is usually set to the
107 diagonal coefficient of the matrix before adding the equation: $c_R = m_P$. By
108 specifying the reference value ψ_R , the solution gets locally constrained in a
109 weak sense. This approach is however extremely sensitive to the smallest errors
110 in the corresponding compatibility condition of the Neumann problem. Such
111 numerical errors may arise from the data exchange between child and parent
112 mesh due to interpolation.

113 A much more robust regularisation can be achieved by inverting the idea
 114 of the so called Hotelling deflation [43], which is actually a simple technique to
 115 solve eigenproblems by selectively shifting single known eigenvalues of a matrix
 116 to zero. Conversely, we may use the same procedure to shift them also from
 117 zero to an arbitrary value, thus inflating the matrix.

According to the spectral theorem for symmetric matrices [44], it is possible
 to decompose \mathbf{M} based on its eigenvalues λ_k and orthonormal eigenvectors \mathbf{v}_k :

$$\mathbf{M} = \sum_{k=1}^n \lambda_k \mathbf{v}_k \mathbf{v}_k^T = \lambda_1 \mathbf{v}_1 \mathbf{v}_1^T + \sum_{k=2}^n \lambda_k \mathbf{v}_k \mathbf{v}_k^T. \quad (20)$$

Using this decomposition we may then create a non-singular matrix $\widetilde{\mathbf{M}}$ using
 only \mathbf{v}_1 from above:

$$\widetilde{\mathbf{M}} = \mathbf{M} + \widetilde{\lambda}_1 \mathbf{v}_1 \mathbf{v}_1^T = \mathbf{M} + \widetilde{\lambda}_1 \frac{1}{n} \mathbf{1} \mathbf{1}^T, \quad (21)$$

where $\widetilde{\lambda}_1$ is any non-zero eigenvalue replacing λ_1 . It is important to note that $\widetilde{\mathbf{M}}$
 does not preserve the original sparsity pattern of \mathbf{M} , which is usually undesired.
 Hence, a direct manipulation would not only mean a waste of memory, but also
 a contraction in terms of the face addressing of OpenFOAM. However, we may
 include the modification indirectly when computing the matrix-vector product:

$$\widetilde{\mathbf{M}}\boldsymbol{\psi} = \mathbf{M}\boldsymbol{\psi} + \widetilde{\lambda}_1 \frac{1}{n} \mathbf{1} \mathbf{1}^T \boldsymbol{\psi} = \mathbf{M}\boldsymbol{\psi} + \widetilde{\lambda}_1 \frac{1}{n} \sum_{k=1}^n \psi_k \mathbf{1}, \quad (22)$$

118 which is essentially the kernel of any iterative equation solver [45]. Furthermore
 119 parallelisation is straight-forward as the exchange of the rightmost sum does
 120 only require little communication.

121 Taking the properties of \mathbf{M} into consideration, it can be shown that all of
 122 its eigenvalues are smaller or equal to twice the maximum of its diagonal coeffi-
 123 cients. Therefore we use the diagonal mean as modified eigenvalue $\widetilde{\lambda}_1 = \langle m_P \rangle$,
 124 thus preserving the spectral radius of \mathbf{M} . Tests with the preconditioned CG-
 125 method [45] showed that the smoothness of the numerical solution is preserved
 126 even if errors in the compatibility condition exist. Compared to the original
 127 regularisation technique in OpenFOAM we could not find any drawbacks.

128 **5. Results**

129 *5.1. Test case 1: speed-up of Biot-Savart’s law*

130 In this section we present a performance analysis of the magnetic field com-
 131 putation in a cylindrical geometry with an imposed current density \mathbf{J} (the other
 132 parts of the solver are switched off). The speedup and scaling analysis is car-
 133 ried out on a cluster with Intel 8-Core Xeon 3,3 GHz CPUs cross linked with
 134 40 Gbit/s Infiniband. The solvers are compiled with OpenFOAM 2.2.0 and MPI
 135 1.6.3.

136 In a first step we solve only Biot-Savart’s law (equation 9) for all cells and
 137 boundary faces – on a changing number of processors. The test case contains
 352 000 cells. Figure 3a shows a good scaling up to 64 processors. The com-

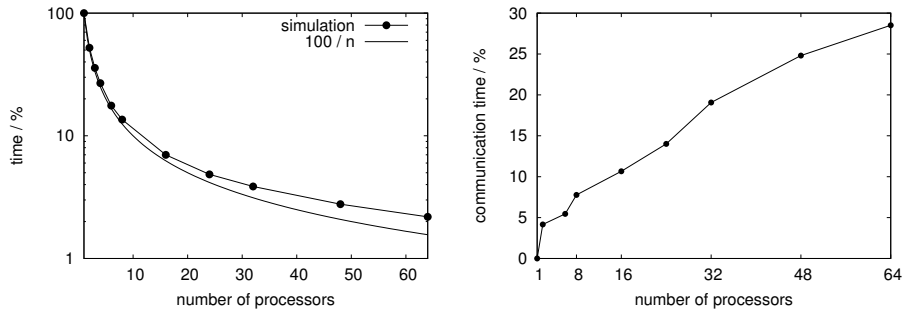


Figure 3: Computation time of Biot-Savart’s law on 1 to 64 processors (a) and communication time divided by total time (b).

138

139 munication time is 28% when using all 64 processors. In that case a single
 140 processor contains only 5500 cells.

141 In a second test case, we use the same configuration again and compare the
 142 full Biot-Savart integral with the method of solving the induction equation 10.
 143 For the latter, we compute Biot-Savart’s law only on the patches in order to
 144 obtain the correct boundary conditions. Figure 4 shows the relative computation
 145 times (total cpu time/(cpu time for simulation in one processor)*100%) for one
 146 to 16 processors. The method of using the Biot-Savart law on the boundary
 147 regions only together with the solution of the corresponding induction equation

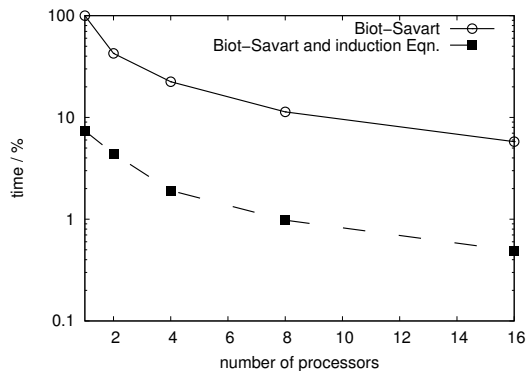


Figure 4: Relative calculation time for the volume based Biot-Savart and the surface based Biot-Savart combined with solving the induction equation.

148 in the inner region scales very well, too; it is approximately 13.5 times faster than
 149 the volume Biot-Savart method. Note that this factor will probably increase for
 150 larger problems with more cells.

151 In a third case we use a mesh with 63 200 cells and compare the magnetic
 152 field with the vector potential approach. In both cases we firstly compute the
 153 boundary conditions and solve then a transport equation for \mathbf{A} or \mathbf{B} on a single
 154 processor 50 times. The fastest result we obtain by using Biot-Savart for the
 155 vector potential (equation 12 and 13). Computing the magnetic field on the
 156 boundary and solving the induction equation (equation 9 and 10) is five times
 157 slower. The volume-based Biot-Savart is 84 times slower. Of course this holds
 158 only for the Biot-Savart calculation; the differences for the whole solver, where
 159 the flow simulation is included, will be smaller.

160 5.2. Test case 2: current distribution in 2D

161 In a second test case the discretisation schemes for electric conductivity and
 162 potential are validated by comparison with the commercial software Opera. We
 163 simulate a simple two-dimensional geometry ($1 \times 2 \times 0.1$ m), consisting of two
 164 conductors of very different conductivity with an inclined surface (inclination
 165 45°) – see figure 5a. A vertical current of 1 A is applied. Figure 5b shows the
 166 equipotential lines, figure 5c the current lines and 5d the disturbed current. As

expected, the current lines concentrate in the area of high conductivity. Figure 6

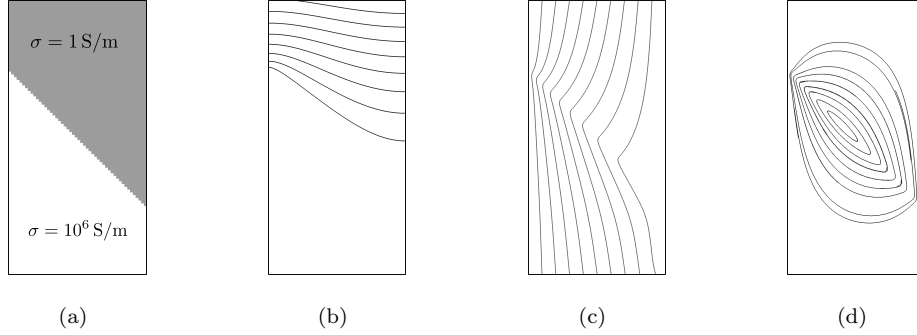


Figure 5: Conductivity (a), electric potential (b), complete current (c) and disturbed current (d). The applied electrical current of 1 A if flowing upwards.

167

168 shows the electric potential and horizontal current along a vertical centred line.

169 The result of OpenFOAM and Opera match very well. Obviously, Opera uses

170 Dirichlet boundary conditions for the electric potential (i.e. an equal-potential surface) – so the same was done in OpenFOAM.

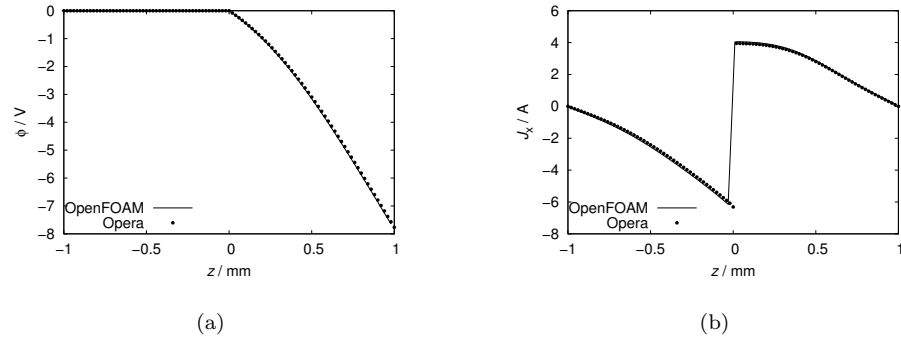


Figure 6: Electric potential (a) and horizontal current (b) along a centered vertical line for an applied current of 1 A.

171

172 5.3. Testcase 3: electro-vortex flow in a cylindrical geometry

173 Several model experiments [46, 47, 48] and similar analytical solutions [49,
174 50] of electro-vortex flow are known from literature with most of them unfortu-
175 nately lacking detailed information. Here we will study the well reviewed exam-

176 ple of a thin electrode touching a cylindrical bath of liquid metal [51, 52, 53].
 177 The experiment was conducted at the Institute of Physics in Riga and pub-
 178 lished by Zhilin et al. [54]. Figure 7 illustrates the setup: a horizontal current
 179 passes through a cylindrical bath of liquid mercury (colored in blue). One cop-
 180 per electrode covers the whole surface, the other is reduced to a small rod. The
 181 whole experiment is embedded into a steel pipe; two mercury filled “buffer zones”
 182 provide for a smooth current transition” between external wires and the exper-
 183 iment. The axial velocity along the cylinder axis is measured with a spacing of
 184 1 mm in x -direction at $y = 0$.

185 Unfortunately, the article does not provide any details about the external
 186 current leads. They are therefore assumed to be infinitely long. The mea-
 187 surements colored in red (fig. 7) were not quoted by Zhilin et al. [54], but
 188 estimated from the sketch. Similarly, the material properties were not given by
 189 [54]; they may vary considerably depending on the exact material/alloy. We
 190 assume the copper conductivity to be $\sigma_{\text{Cu}} = 58.5 \cdot 10^6 \text{ S/m}$, the conductivity of
 191 mercury as $\sigma_{\text{Hg}} = 1.04 \cdot 10^6 \text{ S/m}$ and its density as $\rho_{\text{Hg}} = 13\,534 \text{ kg/m}^3$. The
 192 tube is made of “stainless steel”; we assume therefore an electric conductivity
 193 of $\sigma_{\text{St}} = 1.4 \cdot 10^6 \text{ S/m}$ which is typical for X5CrNi18-10. The tube works as po-
 194 tential divider – only a part of the current passes through the mercury/copper.

195
 196 Figure 8a shows the general flow structure. Assuming infinitely long lateral
 197 current leads and neglecting external magnetic fields, we expect exactly such

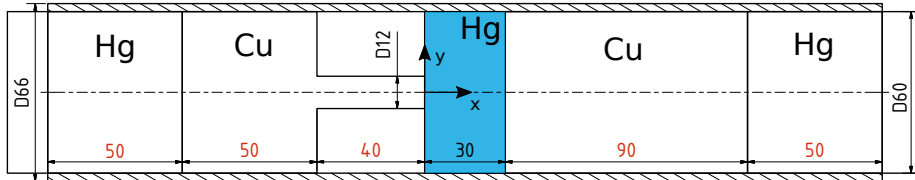


Figure 7: Sketch of the experiment of Zhilin et al. [54]. The experiment is modelled with thick lateral current collectors which are 3 m long. The red dimensions are estimated. The working section (blue) with the symmetry axis x is filled with liquid mercury.

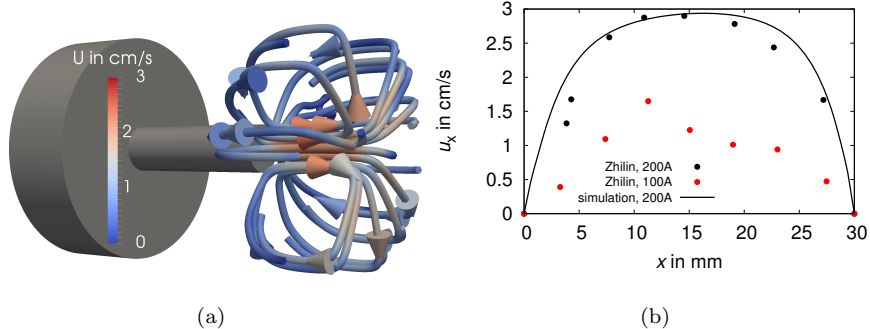


Figure 8: Electro-vortex flow at $I = 200$ A (a) and measured axial velocity at the cylinder axis as given by Zhilin et al. [54] (b).

198 a symmetric flow. Further we expect the velocity along the cylinder axis to
 199 be approximately uniform in the middle of the test section (see black curve in
 200 fig. 8b) as long as the current is not extremely low. The simulated curve for
 201 $I = 200$ A fits very well to the measured velocity values (black dots). A certain
 202 deviation can be explained by the many unknown experimental parameters;
 203 especially the length of the rod has a certain influence on the magnitude of the
 204 flow.

205 The experimental result for $I = 100$ A shows a clear velocity peak shortly
 206 behind the rod (fig. 8b, red dots). This observation can have several reasons:
 207 the jet is oscillating, the jet expands along its way or it is deflected to the side.
 208 As the velocity peak is pronounced especially at low currents, a deflection due to
 209 external magnetic fields is the most probable explanation. Here again, relevant
 210 information about magnetic background fields and positioning of the feeding
 211 cables is missing.

212 6. Summary and outlook

213 We have developed a solver for electro-vortical flow, using a mesh mapping
 214 method. Arbitrary solid and fluid conductors are fully coupled. Electric poten-
 215 tial and current density are solved on a global mesh, and copied to the fluid
 216 mesh. This parent-child mesh technique is much faster than the classical segre-

217 gated approach. A PCG solver with an improved regularisation technique for
218 the Poisson equation of the electric potential helps avoiding numerical errors.
219 The magnetic field is computed fully parallel using Biot-Savart’s law. This was
220 shown to be efficient at least up to 64 processors. Calculating Biot-Savart’s law
221 only on the boundaries and solving a corresponding induction equation in the
222 fluid region speeds up the magnetic field computation drastically. The solver
223 was validated using the commercial software Opera and by comparison with
224 experimental data.

225 The solver presented can easily cope with up to 1 million cells. For larger
226 simulations, a multigrid method or a coarser grid for the magnetic field com-
227 putation might be necessary. Further, the solver shall be compared to recent
228 experimental data. For a meaningful comparison to experimental data, all
229 dimensions of the setup and all conductivities of the conductors as well the
230 placement of the feeding lines and possible magnetic background fields must be
231 known. Only in that case a computation of the experimentally investigated case
232 can successfully be performed. We aim to use the solver to study electro-vortex
233 flow in liquid metal batteries [55, 13] and aluminium reduction cells [56] as well
234 as for related experiments [57, 58].

235 **Acknowledgements**

236 This work was supported by Helmholtz-Gemeinschaft Deutscher Forschungs-
237 zentren (HGF) in frame of the Helmholtz Alliance “Liquid metal technologies”
238 (LIMTECH). The computations were performed on the Bull HPC-Cluster “Tau-
239 rus” at the Center for Information Services and High Performance Computing
240 (ZIH) at TU Dresden and on the cluster “Hydra” at Helmholtz-Zentrum Dres-
241 den - Rossendorf. Fruitful discussions with R. Ashour, S. Beale, V. Bojarevics,
242 D. Kelley, A. Kharicha, J. Priede and F. Stefani on several aspects of electro-
243 vortex flow are gratefully acknowledged. N. Weber thanks Henrik Schulz for the
244 HPC support.

245 **References**

- 246 [1] A. Ludwig, M. Wu, A. Kharicha, Simulation in Metallurgical Processing:
247 Recent Developments and Future Perspectives, JOM 68 (8) (2016) 2191–
248 2197. doi:10.1007/s11837-016-1992-0.
- 249 [2] D. Rübiger, Y. Zhang, V. Galindo, S. Franke, B. Willers, S. Eckert, The
250 relevance of melt convection to grain refinement in Al-Si alloys solidified
251 under the impact of electric currents, Acta Materialia 79 (2014) 327–338.
252 doi:10.1016/j.actamat.2014.07.037.
- 253 [3] S. Franke, D. Rübiger, V. Galindo, Y. Zhang, S. Eckert, Investigations
254 of electrically driven liquid metal flows using an ultrasound Doppler flow
255 mapping system, Flow Measurement and Instrumentation 48 (2016) 64–73.
256 doi:10.1016/j.flowmeasinst.2015.09.004.
- 257 [4] O. V. Kazak, A. N. Semko, Numerical modeling of electro-vortical flows in
258 a confined volume, J. Eng. Phys. Thermophys. 85 (2012) 1167 – 1178.
- 259 [5] A. Kharicha, W. Schützenhöfer, A. Ludwig, R. Tanzer, M. Wu, On the
260 importance of electric currents flowing directly into the mould during an
261 ESR process, steel research international 79 (8) (2008) 632–636.
- 262 [6] A. Kharicha, A. Ludwig, M. Wu, On Melting of Electrodes during Electro-
263 Slag Remelting, ISIJ International 54 (7) (2014) 1621–1628. doi:10.2355/
264 isijinternational.54.1621.
- 265 [7] A. Kharicha, I. Teplyakov, Y. Ivochkin, M. Wu, A. Ludwig, A. Guseva, Ex-
266 perimental and numerical analysis of free surface deformation in an elec-
267 trically driven flow, Experimental Thermal and Fluid Science 62 (2015)
268 192–201. doi:10.1016/j.expthermflusci.2014.11.014.
- 269 [8] H. Zhang, J. Li, Z. Wang, Y. Xu, Y. Lai, The numerical Modeling of Melt
270 Flow and MHD Instabilities in an aluminum Reduction Cell, JOM.

- 271 [9] A. Cramer, G. Gerbeth, P. Terhoeven, A. Krätschmar, Fluid velocity mea-
272 surements in electro-vortical flows, *Mater. Manuf. Process.* 19 (4) (2004)
273 665 – 678.
- 274 [10] O. Kazak, Modeling of Vortex Flows in Direct Current (DC) Electric
275 Arc Furnace with Different Bottom Electrode Positions, *Metallurgical*
276 *and Materials Transactions B* 44 (5) (2013) 1243–1250. doi:10.1007/
277 s11663-013-9899-4.
- 278 [11] N. Weber, V. Galindo, J. Priede, F. Stefani, T. Weier, The influence of
279 current collectors on Tayler instability and electro vortex flows in liquid
280 metal batteries, *Physics of Fluids* 27 (014103).
- 281 [12] F. Stefani, V. Galindo, C. Kasprzyk, S. Landgraf, M. Seilmayer, M. Starace,
282 N. Weber, T. Weier, Magnetohydrodynamic effects in liquid metal batter-
283 ies, *IOP Conference Series: Materials Science and Engineering* 143 (2016)
284 012024. doi:10.1088/1757-899X/143/1/012024.
- 285 [13] T. Weier, A. Bund, W. El-Mofid, G. M. Horstmann, C.-C. Lalau, S. Land-
286 graf, M. Nimtz, M. Starace, F. Stefani, N. Weber, Liquid metal batteries -
287 materials selection and fluid dynamics, *IOP Conf. Ser.: Mater. Sci. Eng.*
- 288 [14] V. Bojarevičs, Y. Freibergs, E. I. Shilova, E. V. Shcherbinin, *Electrically*
289 *Induced Vortical Flows*, Kluwer Academic Publishers, 1989.
- 290 [15] P. A. Davidson, *An Introduction to Magnetohydrodynamics*, Cambridge
291 *texts in applied mathematics*, Cambridge University Press, Cambridge ;
292 New York, 2001.
- 293 [16] A. Y. Chudnovskii, Modeling electrovortex flows, *Magnetohydrodynamics*
294 25 (3) (1989) 337–341.
- 295 [17] J. A. Shercliff, Fluid motions due to an electric current source, *J. Fluid*
296 *Mech.* 40 (1970) 241 – 250.

- 297 [18] H. Rusche, H. Jasak, Implicit solution techniques for coupled multi-field
298 problems – Block Solution, Coupled Matrices (2010).
- 299 [19] S. B. Beale, H. K. Roth, A. Le, D. H. Jeon, Development of an open source
300 software library for solid oxide fuel cells, Tech. Rep. NRCC 53179, National
301 Research Council Canada (2013).
- 302 [20] S. B. Beale, H.-W. Choi, J. G. Pharoah, H. K. Roth, H. Jasak, D. H.
303 Jeon, Open-source computational model of a solid oxide fuel cell, Computer
304 Physics Communications 200 (2016) 15–26. doi:10.1016/j.cpc.2015.10.
305 007.
- 306 [21] P. Beckstein, V. Galindo, V. Vukčević, Efficient solution of 3D elec-
307 tromagnetic eddy-current problems within the finite volume framework
308 of OpenFOAM, Journal of Computational Physics 344 (2017) 623–646.
309 doi:10.1016/j.jcp.2017.05.005.
- 310 [22] N. Weber, V. Galindo, F. Stefani, T. Weier, T. Wondrak, Numerical sim-
311 ulation of the Tayler instability in liquid metals, New Journal of Physics
312 15 (043034).
- 313 [23] M. Seilmayer, F. Stefani, T. Gundrum, T. Weier, G. Gerbeth, M. Gellert,
314 G. Rüdiger, Experimental Evidence for a Transient Tayler Instability in a
315 Cylindrical Liquid-Metal Column, Phys. Rev. Lett. 108 (244501).
- 316 [24] N. Weber, V. Galindo, F. Stefani, T. Weier, Current-driven flow instabilities
317 in large-scale liquid metal batteries, and how to tame them, Journal of
318 Power Sources 265 (2014) 166–173. doi:10.1016/j.jpowsour.2014.03.
319 055.
- 320 [25] W. Herreman, C. Nore, L. Cappanera, J.-L. Guermond, Tayler instability in
321 liquid metal columns and liquid metal batteries, Journal of Fluid Mechanics
322 771 (2015) 79–114. doi:10.1017/jfm.2015.159.
- 323 [26] V. Bandaru, T. Boeck, D. Krasnov, J. Schumacher, A hybrid finite dif-
324 ference–boundary element procedure for the simulation of turbulent MHD

- 325 duct flow at finite magnetic Reynolds number, *Journal of Computational*
326 *Physics* 304 (2016) 320–339.
- 327 [27] A. J. Meir, P. G. Schmidt, A velocity-current formulation for stationary
328 MHD flow, *Applied Mathematics and Computation* 65 (1994) 95 – 109.
- 329 [28] A. J. Meir, P. G. Schmidt, Variational methods for stationary MHD flow
330 under natural interface conditions, *Nonlinear Analysis: Theory, Methods*
331 *& Applications* 26 (1996) 659 – 689.
- 332 [29] P. G. Schmidt, A Galerkin method for time-dependent MHD flow with
333 non-ideal boundaries, *Commun. Appl. Anal.* 3 (1999) 383 – 398.
- 334 [30] A. J. Meir, P. G. Schmidt, Analysis and finite element simulation of mhd
335 flows, with an application to liquid metal processing, in: *Fluid Flow Phen-*
336 *omena in Metals Processing*, 1999, pp. 561 – 569.
- 337 [31] A. J. Meir, P. G. Schmidt, Analysis and numerical approximation of a sta-
338 tionary mhd flow problem with nonideal boundary, *Siam J. Numer. Anal.*
339 34 (1999) 1304 – 1332.
- 340 [32] A. J. Meir, P. G. Schmidt, S. I. Bakhtiyarov, R. A. Overfelt, Numerical
341 simulation of steady liquid – metal flow in the presence of a static magnetic
342 field, *Journal of Applied Mechanics* 71 (6) (2004) 786 – 795.
- 343 [33] M. Xu, F. Stefani, G. Gerbeth, Integral equation approach to time-
344 dependent kinematic dynamos in finite domains, *Phys. Rev. E* 70 (2004)
345 056305.
- 346 [34] M. Xu, F. Stefani, G. Gerbeth, The integral equation method for a steady
347 kinematic dynamo problem, *J. Comput. Phys.* 196 (2004) 102 – 125.
- 348 [35] M. Xu, F. Stefani, G. Gerbeth, The integral equation approach to kinematic
349 dynamo theory and its application to dynamo experiments in cylindrical
350 geometry, *J. Comput. Phys.* 227 (2008) 8130–8144.

- 351 [36] N. Weber, V. Galindo, F. Stefani, T. Weier, The Tayler instability at low
352 magnetic Prandtl numbers: Between chiral symmetry breaking and helicity
353 oscillations, *New Journal of Physics* 17 (11) (2015) 113013. doi:10.1088/
354 1367-2630/17/11/113013.
- 355 [37] F. Stefani, A. Giesecke, N. Weber, T. Weier, Synchronized Helicity Oscilla-
356 tions: A Link Between Planetary Tides and the Solar Cycle?, *Solar Physics*
357 291 (8) (2016) 2197–2212. doi:10.1007/s11207-016-0968-0.
- 358 [38] L. A. Santalo, *Vectores y Tensores Con Sus Aplicaciones*, Universidad de
359 Buenos Aires, Buenos Aires, 1993.
- 360 [39] N. Weber, P. Beckstein, V. Galindo, W. Herreman, C. Nore, F. Stefani,
361 T. Weier, Metal pad roll instability in liquid metal batteries, *Magneto-*
362 *hydrodynamics* 53 (1) (2017) 129–140.
- 363 [40] N. Weber, P. Beckstein, W. Herreman, G. M. Horstmann, C. Nore, F. Ste-
364 fani, T. Weier, Sloshing instability and electrolyte layer rupture in liquid
365 metal batteries, *Physics of Fluids* 29 (5) (2017) 054101. doi:10.1063/1.
366 4982900.
- 367 [41] R. Moreau, *Magneto hydrodynamics*, Kluwer Academic Publishers, 1990.
- 368 [42] R. I. Issa, Solution of the Implicit Discretised Fluid Flow Equations by
369 Operator-Splitting, *Journal of Computational Physics* 62 (1985) 40 – 65.
- 370 [43] J. H. Wilkinson, *The Algebraic Eigenvalue Problem*, Oxford University
371 Press, Oxford, 1965.
- 372 [44] B. N. Parlett, *The Symmetric Eigenvalue Problem*, Society for Industrial
373 and Applied Mathematics, 1998. doi:10.1137/1.9781611971163.
- 374 [45] Y. Saad, *Numerical Methods for Large Eigenvalue Problems*, rev. ed Edi-
375 tion, no. 66 in *Classics in applied mathematics*, Society for Industrial and
376 Applied Mathematics, Philadelphia, 2011.

- 377 [46] R. A. Woods, D. R. Milner, Motion in the weld pool in arc welding, *Welding*
378 *Journal* 50 (1971) 163–s.
- 379 [47] A. I. Dementev, A. I. Chaikovskii, A. Y. Chudnovskii, Generation of elec-
380 trovortex flows in liquid-metal baths with a multielectrode current input,
381 *Magnetohydrodynamics* 24 (1) (1988) 76–80.
- 382 [48] S. B. Dement'ev, O. M. Skopis, E. V. Sherbinin, Intensification of the mix-
383 ing process in direct-current electric arc furnaces, *Magnetohydrodynamics*
384 28 (1) (1992) 89–92.
- 385 [49] I. E. Butsenieks, D. E. Peterson, V. I. Sharamkin, E. V. Sherbinin, Mag-
386 netohydrodynamic fluid flows in a closed space with a nonuniform electric
387 current, *Magnitnaya Gidrodinamika* 1 (1976) 92 – 97.
- 388 [50] R. P. Millere, V. I. Sharamkin, E. V. Shcherbinin, Effect of a longitudinal
389 magnetic field on electrically driven rotational flow in a cylindrical vessel,
390 *Magnitnaya Gidrodinamika* 1 (1980) 81 – 85.
- 391 [51] V. N. Moshnyaga, V. I. Sharamkin, Experimental investigation of electro-
392 vortical flow in a cylindrical vessel, *Magnetohydrodynamics* 16 (1) (1980)
393 62–65.
- 394 [52] L. A. Volokhonskii, Dynamic boundary layer of electrovortex flow in a cylin-
395 drical volume with axisymmetric current supply, *Magnetohydrodynamics*
396 27 (4) (1991) 467–470.
- 397 [53] A. Y. Chudnovskii, Evaluating the intensity of a single class of electrovortex
398 flows MHD, *Magnetohydrodynamics* 25 (3) (1989) 406–408.
- 399 [54] V. G. Zhilin, Y. P. Ivochkin, A. A. Oksman, G. R. Lurin'sh, A. I.
400 Chaikovskii, A. Y. Chudnovskii, E. V. Shcherbinin, An experimental in-
401 vestigation of the velocity field in an axisymmetric electrovortical flow in a
402 cylindrical container, *Magnitnaya Gidrodinamika* 3 (1986) 110 – 116.

- 403 [55] H. Kim, D. A. Boysen, J. M. Newhouse, B. L. Spatocco, B. Chung, P. J.
404 Burke, D. J. Bradwell, K. Jiang, A. A. Tomaszowska, K. Wang, W. Wei,
405 L. A. Ortiz, S. A. Barriga, S. M. Poizeau, D. R. Sadoway, Liquid Metal
406 Batteries: Past, Present, and Future, *Chemical Reviews* 113 (3) (2013)
407 2075–2099. doi:10.1021/cr300205k.
- 408 [56] J. W. Evans, D. P. Ziegler, The Electrolytic Production of Aluminum,
409 in: A. Bard, M. Startmann (Eds.), *Electrochemical Engineering*, Vol. 5 of
410 *Encyclopedia of Electrochemistry*, Wiley-VCH, Weinheim, 2007, pp. 224–
411 265, volume editors: Macdonald, D.D. and Schmuki, P.
- 412 [57] M. Starace, N. Weber, M. Seilmayer, T. Weier, F. Stefani, S. Eckert, Ultra-
413 sound Doppler flow measurements in a liquid metal column under the in-
414 fluence of a strong axial electric current, *Magnetohydrodynamics* 51 (2015)
415 249 – 256.
- 416 [58] D. H. Kelley, D. R. Sadoway, Mixing in a liquid metal electrode, *Physics*
417 *of Fluids* 26 (5) (2014) 057102. doi:10.1063/1.4875815.